

The 3D Attenuation Structure of Deception Island (Antarctica)

J. Prudencio^{1,2,3} · L. De Siena^{4,5} · J. M. Ibáñez^{1,2,6} ·
E. Del Pezzo^{1,7} · A. García-Yeguas^{1,3,8} · A. Díaz-Moreno^{1,2,3}

Received: 16 July 2014 / Accepted: 2 March 2015 / Published online: 14 March 2015
© Springer Science+Business Media Dordrecht 2015

Abstract The seismic and volcanological structure of Deception Island (Antarctica) is an intense focus topic in Volcano Geophysics. The interpretations given by scientists on the origin, nature, and location of the structures buried under the island strongly diverge. We present a high-resolution 3D *P*-wave attenuation tomography model obtained by using the coda normalization method on 20,293 high-quality waveforms produced by active sources. The checkerboard and synthetic anomaly tests guarantee the reproduction of the input anomalies under the island down to a depth of 4 km. The results, once compared with our current knowledge on the geological, geochemical, and geophysical structure of the region, depict Deception as a piecemeal caldera structure coming out of the Bransfield Trough. High-attenuation anomalies contouring the northeastern emerged caldera rim correlate with the locations of sediments. In our interpretation, the main attenuation contrast, which appears under the collapsed southeastern caldera rim, is related to the deeper feeding systems. A

✉ L. De Siena
lucadesiena@abdn.ac.uk

J. Prudencio
janire@ugr.es

¹ Instituto Andaluz de Geofísica, University of Granada, Profesor Clavera 12, 18071 Granada, Spain

² Dept. Física Teórica y del Cosmos, University of Granada, Fuentenueva S/N, 18001 Granada, Spain

³ INVOLCAN, Antiguo Hotel Taoro, Parque Taoro 22, 38400 Puerto de la Cruz, Tenerife, Spain

⁴ Institut für Geophysik, University of Münster, Correnstrasse 24, 48149 Münster, Germany

⁵ School of Geosciences, Geology and Petroleum Geology, Meston Building, University of Aberdeen, King's College, Aberdeen AB24 3UE, Scotland, UK

⁶ Sezione di Catania -Osservatorio Etneo, Istituto Nazionale di Geofisica e Vulcanologia, 95125 Catania, Italy

⁷ Sezione di Napoli -Osservatorio Vesuviano, Istituto Nazionale di Geofisica e Vulcanologia, Via Diocleziano 328, 80124 Naples, Italy

⁸ Dept. Física Aplicada, University of Cádiz, Av. Duque de Nájera 18, 11002 Cádiz, Spain

unique *P*-wave high-attenuation spherical-like anomaly in the inner bay extends between depths of 1 and 3 km. The northern contour of the anomaly coincides with the calderic rim both at 1 and 2 km, while smaller anomalies connect it with deeper structures below 3 km, dipping toward the Bransfield Trough. In our interpretation, the large upper anomaly is caused by a high-temperature shallow (1–3 km deep) geothermal system, located beneath the sediment-filled bay in the collapsed blocks and heated by smaller, deeper contributions of molten materials (magma) rising from southeast.

Keywords Attenuation · Scattering · Tomography · Antarctica

1 Introduction

Deception Island (Fig. 1) is considered as a laboratory for Volcano Geophysics due to the large number of multidisciplinary studies focused both on imaging its surface and deep structures and on monitoring its volcanic activity. Scientists have widely studied the origin and morphology of Deception Island, bringing forward general and local models (e.g., Martí et al. 1996, 2013; Smellie et al. 2002; Fernández-Ibáñez et al. 2005; Maestro et al. 2007; Barclay et al. 2009; Melo et al. 2012; Torrecillas et al. 2012, 2013). The study of the seismic activity of the volcano is probably the most active and productive research line, as reported by Tejedo et al. (2014). There are many results that help us better understand the dynamic and volcanological framework of the area, such as Vila et al. (1992), Almendros et al. (1997), Ibáñez et al. (1997, 2000, 2003), Saccorotti et al. (2001), Martínez-Arevalo et al. (2003), Benitez et al. (2007), Carmona et al. (2010, 2012, 2014), and García-Yeguas et al. (2010). One of the objectives of these seismic studies is to provide 2D or 3D structure of the area, by using active or passive data as has been done by Ben-Zvi et al. (2009), Zandomenoghi et al. (2009), and Prudencio et al. (2013). These seismic models have been used to confirm or help to build other geophysical or geodynamic models of the island, such as magnetotelluric (Pedrera et al. 2012), geomagnetic (Muñoz Martín et al. 2005), gravimetric (Catalan et al. 2006), or geodetic (Berrocoso et al. 2012; Prates et al. 2013). Additionally, geochemical analysis of the composition and ratio of stable isotopes and gases produced by fumaroles (Caselli et al. 2004, 2007; Kusakabe et al. 2009) are also very well known and provide important information on the presence and origin of magma and fluids. Nowadays, with these observables, the research community is working to provide a geodynamic and volcanological model that could unify all of them in a single interpretation, such as those made by Smellie (2001), Martí et al. (2013), Berrocoso et al. (2012) and Pedrera et al. (2012).

The imaging of region-specific velocity and attenuation through direct-wave tomography provides striking results at local, regional, and global scales (e.g., Schurr et al. 2003; Eberhart-Phillips et al. 2008). Attenuation tomography is today a standard technique, and several codes include this important measurement in their tomographic algorithms (Lees and Lindley 1994; Schurr et al. 2003; Hansen et al. 2004; Eberhart-Phillips et al. 2008; Koulakov et al. 2010). Due to the higher sensitivity of the attenuation parameters to the presence of fluids and melt with respect to velocity, attenuation tomography may provide decisive data to discriminate the location and nature of the volcanic and seismic structures under Deception Island.

incoherent radiation (coda waves, e.g., Sato et al. 2012), affected by dispersion as well as by interference, diffraction, and resonant effects. The coherency in the corresponding direct signals is also quickly lost (La Rocca et al. 2001; Chouet 2003; De Siena et al. 2013). In these media, we may retrieve P - and S -wave attenuation parameters independently of the site and instrumental transfer functions by using the coda normalization method (Aki and Richards 1980; Yoshimoto et al. 1993; Sato et al. 2012). In recent years, this method has been applied to S -wave attenuation tomography at local scale, exploiting the strong scattering effects produced by strong heterogeneity in volcanic regions (Del Pezzo et al. 2006; Matsumoto et al. 2009; Sato et al. 2012; De Siena et al. 2010).

The coda normalization method is based on the equation that correlates the ratio between the S -wave direct energy and the coda wave energy to the spatial distribution of the inverse total quality factors calculated along the source-station ray-path (Del Pezzo et al. 2006; De Siena et al. 2009, 2014). If active sources are available, the spatial distribution of P -wave attenuation becomes the only unknown in the final coda normalization inverse problem, that is, the method may be exploited at best.

In this study, we obtain the P -wave total quality factor (Q_p), which measures the anelastic and scattering losses suffered by P -waves while propagating into the medium. This quantity provides information on the physical, chemical, and geological state of the Earth and becomes especially useful if compared with seismic velocities. A wide range of physical properties must be considered before discussing the joint results of velocity and attenuation tomography. Their combined interpretation is a decisive tool in discriminating volumes either permeated by fluids or characterized by structural discontinuities (Schurr et al. 2003; Eberhart-Phillips et al. 2008; De Siena et al. 2010).

The relation between velocity and attenuation is often ambiguous. High attenuation and low velocity do not always mean the presence of melt in volcanoes, as fluids, gases, faults, and, more generally, unconsolidated materials (like sediments) all produce high attenuation in the presence of different velocity signatures (Haberland and Rietbrock 2001; Schurr et al. 2003; Hansen et al. 2004; De Siena et al. 2010; Muksin et al. 2013). Several authors (e.g., Priyono et al. 2011) suggest that high ΔQ_p^{-1} and low ΔV_p^{-1} in volcanic regions are related to a magmatic system, while others (e.g., Takanami et al. 2000) relate these correlations to high-temperature zones without partial melting.

The P -to- S velocity ratio (V_p/V_s) is a decisive parameter to discriminate magma from either fluids or gases if spatially correlated with high attenuation (Hansen et al. 2004; Vanorio et al. 2005; De Siena et al. 2010; Kuznetsov and Koulakov 2014). Low V_p/V_s anomalies and high attenuation may in fact be associated with the presence of gas filling faults and fractures, hydrothermal basins, and CO_2 emission beneath volcanoes, mountain ranges, and geothermal reservoirs (Julian et al. 1996, 1998; Hunsen et al. 2004; Hansen et al. 2004). The correlation of high V_p/V_s with high attenuation is critical to discriminate fluids from melt. As no V_p/V_s ratio information is available at Deception Island, other geophysical, geological, and geochemical information must be considered with care in the final interpretation.

The aim of this study is to obtain reliable 3D frequency-dependent P -wave attenuation images of the upper 4 km beneath Deception Island (South Shetland archipelago, Antarctica) by using a subset of the waveforms employed by Ben-Zvi et al. (2009) and Zandomenghi et al. (2009) to obtain velocity tomography results. We will provide new evidences that can be used in the future in a new geophysical interpretation by the comparison of the velocity and attenuation results with the current and new scientific results focused on the formation and structure of the Island.

2 Deception Island: Volcanological and Geophysical Models

Deception Island is an active volcanic island composed of rocks that date to <0.75 Ma and which suffered several historical eruptions in the last two centuries (Smellie 2001) (Fig. 1). Nowadays, its volcanic activity mainly consists of hot hydrothermal waters, fumarolic fields, and intense seismic activity composed by volcanic tremor, persistent long-period, and volcano-tectonic seismicity (Vila et al. 1992; Ortiz et al. 1997; Ibáñez et al. 2000; Carmona et al. 2012).

As indicated above, many of the present efforts of several researchers are focused on the interpretation of the geophysical, geodetic, and geochemical observations in terms of structural and volcanological framework of the volcano to understand its past and to infer a possible evolution and volcanic dynamic. These researchers integrated seismic observations, mainly low and high seismic velocities and contrast in attenuation, conductivity, gases, and geodetical information. On the basis of these observations, there are mainly at the present two possible models that are coincident in the interpretation of the shallower structure (0–2 km) and they are in disagreement with the interpretation of the deeper structure. In one of them, the effects of fractured rocks and the existence of a geothermal system that hydrothermally altered the medium are detected up to 6 km depth (Martí et al. 2013). In the other, the observed anomalies are interpreted as the effects of the presence of a certain amount of melted rock/material with variable volume (e.g., Ben-Zvi et al. 2009; Pedrera et al. 2012; Muñoz Martín et al. 2005).

2.1 Deep Geothermal Effect

Recently, Martí et al. (2013) on the basis of new stratigraphy and petrological studies, with the revision of previous results, proposed a model of the formation and internal structure of the Island. In reference to the present internal structure, the authors show that a polygonal structural network consisting of several preexisting major normal faults controlled pre- and post-caldera volcanism on the island. They defend the formation of the caldera caused the destruction of the associated magma chamber and, hence, recent eruptions have been fed by small batches of deeper-source magma. In their interpretation, a large hydrothermal system developed in the interior of the depression using highly fractured pre-caldera basement and syn-caldera rocks. The authors suggested the current hydrothermal system inside its depression, which may be responsible for most of the present-day observations up to 6 km depth.

2.2 Existence of Melted Material

Most of the geophysical and geodetic studies performed in the area observed the existence of high contrast of the physical properties studied, and these anomalies have an evident presence in the central part of the island (below Port Foster). These anomalies extend up to 6–10 km depth, and their interpretations include the existence of partially melted rocks at depths 2–10 km.

2.2.1 Seismic Velocity Observations

Ben-Zvi et al. (2009) and Zandomenighi et al. (2009) used the dataset provided by the TOMODEC active seismic experiment to obtain 2D and 3D images of *P*-wave velocity structure in the entire area of Deception Island between depth of 0–10 km. Their results

show strong deep (down to 8 km) lateral velocity variations, which are attributed to the presence of crustal magmatic systems with either partially melted regions and frozen intrusive bodies or sediment thickness variations and geothermal systems. The authors identified a large high-velocity anomaly intersecting the northwestern part of Deception Island (Telefon Bay, Fig. 1) that was associated with the crystalline basement of the South Shetland Island platform. However, the main feature of the velocity models is an extended low P -wave velocity anomaly, which intersects both Port Foster bay and the eastern part of the island (Fig. 1). The same authors interpret the shallow low-velocity anomalies (0–2 km) as the effect of sediment-filled basin, hydrothermal activities, fractured materials from the caldera collapse and others. Ben-Zvi et al. (2009, p. 78) on the basis of numerical simulations observed that the velocity anomalies below 2 km depths are compatible with the presence of partially melted materials (up to 15 % melted) and with a maximum volume of up to 20 km³. Zandomeneghi et al. (2009) agree with this interpretation.

2.2.2 Seismic Attenuation Observations

Regarding seismic attenuation, Vila et al. (1995) obtained local attenuation parameters from both coda analysis and source parameter information. The authors show abnormally low coda Q values characterized by high frequency dependence in the inner bay of the island. They do interpret it as due to a hot magmatic intrusion produced during the most recent eruption, but the width of this intrusion is estimated to be only about 0.2 km³. More recently, Martínez-Arevalo et al. (2003) estimated the seismic attenuation of both P - and S -waves at Deception Island, observing a predominance of scattering over intrinsic attenuation. They do interpret these results as produced by a zone of strong heterogeneity, as done in most volcanic areas (Del Pezzo 2008), where the presence of magma patches cannot be excluded. Recently, Prudencio et al. (2013) obtained the regional 2D distribution of intrinsic and scattering attenuation of the Island by using the same waveform dataset employed to image its velocity structure and the diffusion model. The authors confirm the presence of a high scattering attenuation body below the inner bay of Deception Island, strongly interacting with the coda wave field, and which may be compatible with the existence of magma.

2.2.3 Gravimetric and Magnetotelluric Observations

Muñoz Martín et al. (2005) show a very low density anomaly in both magnetic and gravity anomaly maps of Deception Island. The authors interpreted this anomaly as a partially melted intrusive body, and they estimated the top of this body at 1.7 km depth using Euler deconvolution techniques. The 3D resistivity models of Pedrera et al. (2012) reveal an elongated conductor between 2 and 10 km east of Whalers Bay (Fig. 1), which they interpret as induced by a combination of partial melt and hot fluids. The inferred deep magma sill is connected to the surface by a large resistive path ending at Port Foster, interpreted as a shallow magma chamber.

3 Data, Method, and Inversion Setting

3.1 Data and Ray Tracing

The waveforms used in this study are a subset of the ones used by Zandomeneghi et al. (2009) to obtain 3D velocity images by using a shortest-time ray tracing and a LSQR

algorithm inversion. The authors choose two different model parameterizations. The first grid has coarser parameterization (250 m), which is centered on Deception Island and extends 53 km from West to East (WE), 52 km from South to North (SN), and down to 12 km depth. A smaller grid of 100 m step includes Port Foster and the nearest surroundings and extends 12 km WE, 14 km SN, and down to 7 km depth. In order to compare the velocity and attenuation models, we use a grid having the same lateral extension of the first grid in Zandomenighi et al. (2009).

Amplitude data are strongly frequency dependent. We show four recordings produced by a shot in the center of the bay (blue star) and registered at stations M, F, J, and H (Fig. 2). The stations record waveforms with excellent signal-to-noise ratios (larger than 10) for the entire signal above 8 Hz only. However, both Vila et al. (1995) and Prudencio et al. (2013) show abnormally low attenuation values at high frequencies in the Port Foster bay, where we focus our attention. Due to this strong attenuation, we cannot provide reliable attenuation models of structures as deep as 4 km at frequencies larger than 10 Hz.

We obtain the attenuation model after filtering data in the 4–8 frequency band (6 Hz, central frequency). Considering the lowest measured velocities in the inner bay, the signal wavelength associated with this frequency band safely allows us to depict structures of the order of 1 km dimension at 4 km depth. As shown by Prudencio et al. (2013), this frequency band also provides stable results for the separate measurements of both intrinsic and scattering attenuation from coda wave data.

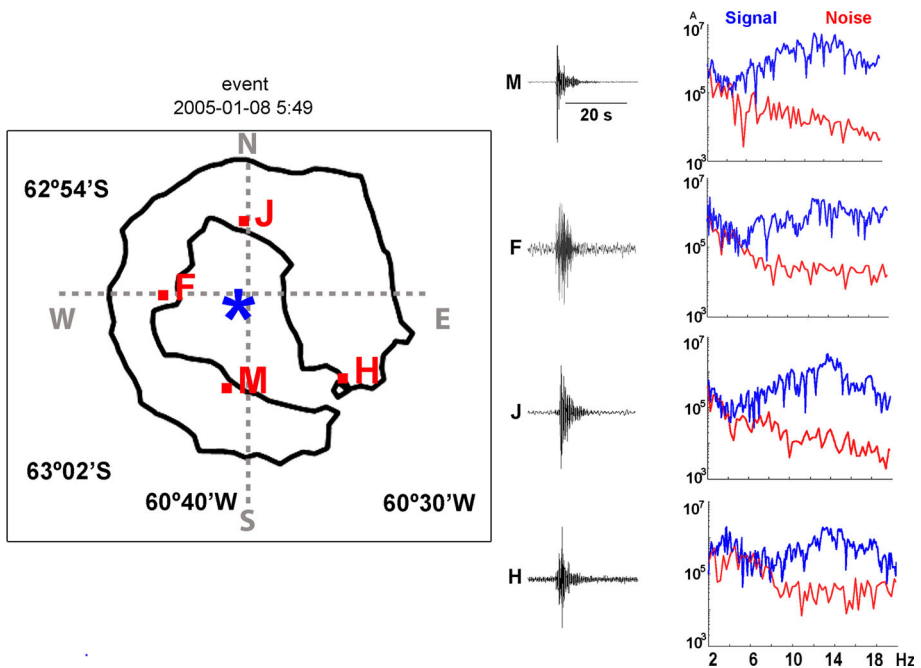


Fig. 2 The vertical records of a seismic shot produced on January 8, 2005, located in the center of the Port Foster bay (blue star), and recorded at four seismic land stations (*M, F, J, H*). The gray dotted line crossing near the center of the bay indicates the location and direction of the vertical sections shown in Fig. 6. The panels on the right show the signal spectrum (*S*, blue lines) and noise spectrum (*N*, red lines) for each recording

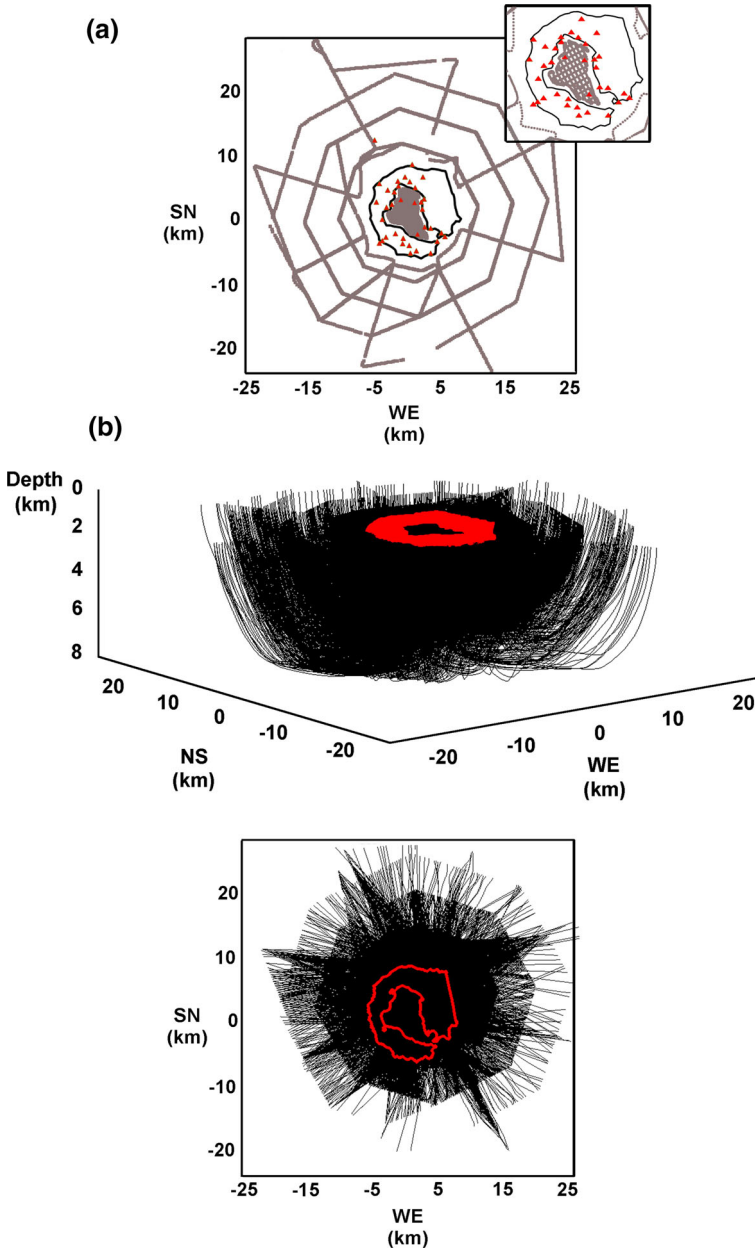


Fig. 3 Configuration of the TOMODEC seismic tomography experiment. **a** Land and ocean bottom seismometers (red triangles) and shot locations (gray lines) are drawn on a contour map of the island. In the *top-right* panel, we zoom in on the center of the island (Port Foster bay). **b** 3D and 2D source-station ray-paths obtained by using a Thurber-modified ray-bending approach. All the events are approximately located at 0 km depth and produced by air guns. The *red contour* map imposed on the rays shows the location and shape of Deception Island with respect to the experiment setting

We use the same Thurber-modified ray-bending approach described, e.g., by De Siena et al. (2010) in the 3D sparse velocity model of Zandomenighi et al. (2009) (Fig. 3). The space density of the rays at a depth of 5 km is still sufficient for correctly performing the tomography inversion (Fig. 3). On the other hand, observational data associated with these paths show highly incoherent estimates even for paths crossing almost the same volumes. Therefore, our analysis and final interpretation are restricted to depths of 1–4 km. These analyses may hint at deeper structures when compared with other measurements.

3.2 *P*-Wave Attenuation Tomography with the Coda Normalization Method

The coda normalization (CN) method has been first applied to the single-station estimate of the total *S*-wave inverse quality factor Q along the seismic path by Del Pezzo et al. (2006) in the Mount Vesuvius volcanic area. The single-path attenuation is obtained in a given frequency range with central frequency f_c by measuring the direct-*S* energy (E_k^s) and the coda *S* energy in a time window centered on a given lapse time $t_c(E_k^c(f_c, t_c))$, and calculating their ratio. The single-path CN equation is:

$$\frac{1}{\pi f_c} \ln \left(\frac{E_k^s(f_c)}{E_k^c(f_c, t_c)} \right) = K(f_c, t_c, \theta, \phi) - \frac{2}{\pi f_c} \gamma \ln(r_k) - 2 \int_{r_k} \frac{dl}{v(l)Q(l)} \quad (1)$$

where r_k is the total length of the k th ray, γ is the geometrical spreading, and $v(l)$ is the velocity of the medium measured along the ray-path. $K(f_c, t_c, \theta, \phi)$ takes into account the effect of the source radiation pattern, described by the takeoff angle (θ) and azimuth (ϕ) and is the only other unknown variable (apart from Q) in the equation. As in given frequency bands, diffraction effects, waveguides, and surface waves could affect the exponent γ of the geometrical spreading, we choose to invert this parameter with the inverse average quality factor (La Rocca et al. 2001; Morozov 2011; De Siena et al. 2014).

As shown by Yoshimoto et al. (1993), we can extend the CN method to the measurement of *P*-wave average attenuation (the *P*-wave quality factor, Q_p). We use active sources, that is, only *P*-waves are produced. We can reasonably assume a spherical source radiation pattern, hence, $K(f_c, t_c, \theta, \phi) = K(f_c, t_c)$, leaving Q_p as the only unknown in the inversion problem. We can thus apply the CN method to *P*-wave attenuation tomography under three assumptions:

- the small *P*- and *S*-wave mean free paths in the volcanic structures allow for a quick conversion of *P*-wave energy into coda energy,
- the seismic paths traveled by the waves producing the energy ratios filtered in the chosen frequency band can be approximated by a ray (curve),
- the lapse time from origin is large enough to measure coda energy out of the *P*-wave transient regime.

The energy ratios versus travel times behavior reveal no evident anomalous energy ratio increase localized in space at 6 Hz, indicative of anomalous coherent effects in the coda envelopes (De Siena et al. 2014). As the lapse time t_c strongly influences the estimates of the average parameter if it is set to short lapse times (Calvet and Margerin 2013), we set the start of the coda time window of length 3 s to a lapse time of 12 s. The *P*-energy time window is set to 1.5 s. The waveforms were selected depending on the coda-to-noise ratio (always larger than 1.5) at 6 Hz.

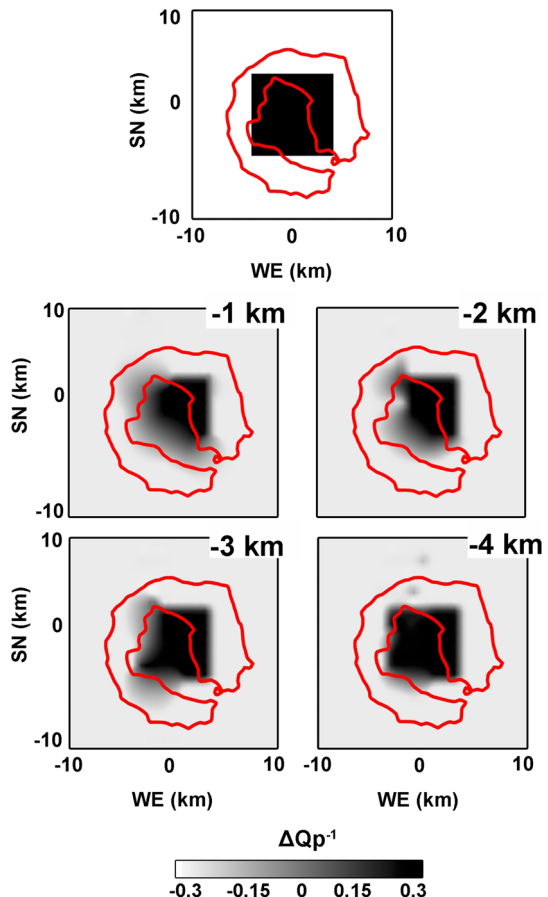
The final dataset is comprised of 20,293 vertical seismic waveforms. The inversion of the energy ratios for the average parameters provides an average Q_p of 29. In the following, we

will discuss the variations with respect to the inverse of the average quality factor in the 3D space (ΔQ_p^{-1}), a direct measurement of attenuation. By considering these observations as well as the ideal distribution of our sources, we invert the energy ratios for the attenuation parameters with the MuRAT code in a single-step inversion (De Siena et al. 2014).

4 Synthetic Tests

We want to discriminate the resolution we effectively achieve on a high-attenuation anomaly in the center of the bay down to 4 km depth (Fig. 4). We start testing the resolution of the ΔQ_p^{-1} results, assuming as input synthetic anomaly a high-attenuation region in the center of the island, roughly designed on the results of the velocity tomography (Fig. 4, high attenuation correlated with high velocity). Hence, we impose a $8 \times 8 \times 4 \text{ km}^3$ volume of low quality factor under Port Foster. We generate synthetic P -to-coda energy ratios, and we add Gaussian random error with zero mean and three times the standard deviation, equal to the 20 % of the data value. We invert the synthetic data only in blocks crossed by at least five rays. We show the results on four horizontal slices at different depths (Fig. 4).

Fig. 4 *Upper panel* The synthetic anomaly test input is designed to show the reproducibility of a simplified deep high-attenuation anomaly under the Port Foster bay. The high-attenuation anomaly has a dimension of $8 \times 8 \times 4 \text{ km}^3$ and is characterized by a quality factor of 3. *Lower panels* Four horizontal slices through the output of the synthetic anomaly test taken at different depths with respect to the sea level. The ΔQ_p^{-1} gray scale shows the variations with respect to the average quality factor



In order to test the resolution in the entire region, we also perform a checkerboard test, whose output is shown on the same four horizontal slices used in Fig. 4 (Fig. 5, third column). We add the same amount of Gaussian random error to the synthetic P -to-coda energy ratios calculated from a checkerboard synthetic structure with 2 km node spacing, starting at 0 km and having quality factors equal to either 100 or 1000. The checkerboard and synthetic anomaly test inputs and outputs are also shown on SN and WE vertical sections, crossing the inner bay (Fig. 3, dotted gray line).

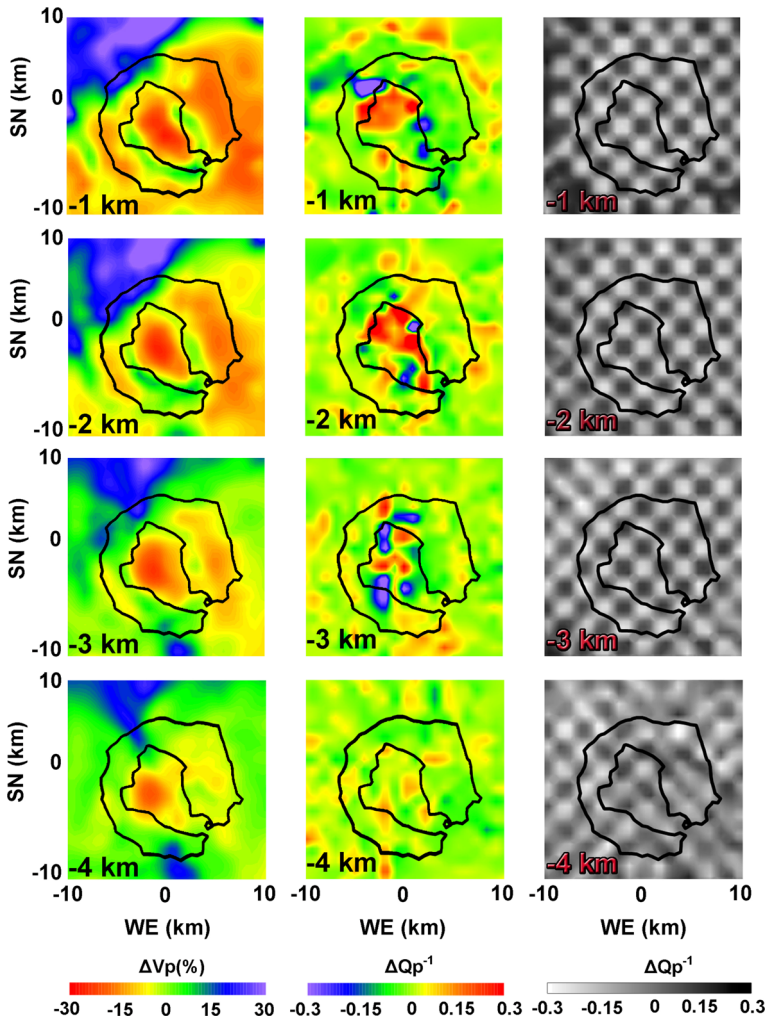


Fig. 5 The results of velocity tomography (Zandomenighi et al. 2009, left-hand column) of the attenuation tomography (central column) and the output of the checkerboard test (right-hand column) are shown on four horizontal slices taken at different depths. The left-hand color scale shows the percent variations of the velocity model with respect to its average. Both the central color scale and the right-hand gray scale show the variations of the attenuation model with respect to the average quality factor. The contour of Deception Island is over-imposed on each panel

The checkerboard test results are well resolved everywhere between depths of 1 and 3 km, while smearing affects the output at 4 km depth, especially in the regions contouring the island (Fig. 5). The synthetic anomaly test is well resolved down to 4 km depth except for some smoothing on the southern and western sides of the images, between depths of 1–3 km (Figs. 4, 6). We conclude that we have good resolution in the volume under study.

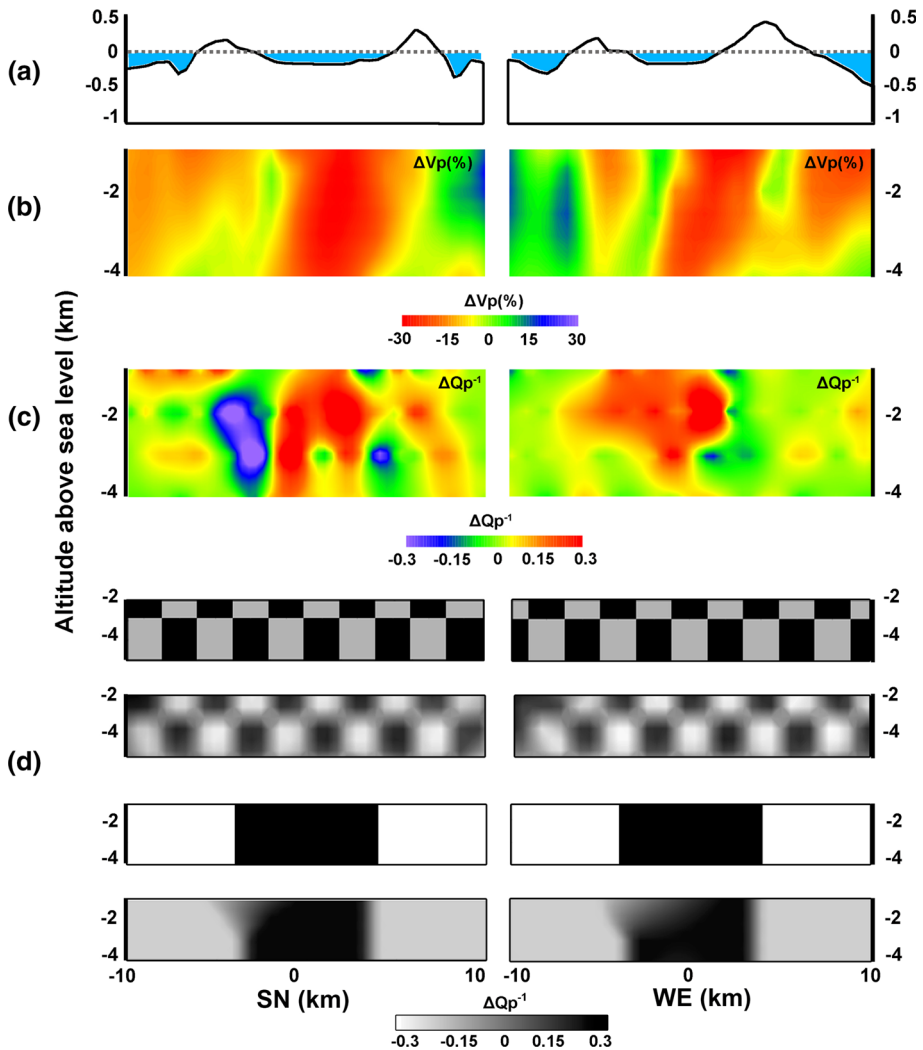


Fig. 6 Bathymetry (a), velocity model (Zandomeneghi et al. 2009, b), attenuation model (c), and the synthetic tests (d) are all shown on two vertical sections crossing the Island (gray dotted lines in Fig. 3). The vertical scale in the velocity and attenuation images is enlarged for clarity. **b** The color scale shows the percent variations of the velocity model with respect to its average. **c** The color scale shows the variations of the attenuation model with respect to the average quality factor. **d** The ΔQ_p^{-1} gray scale shows the variations with respect to the average quality factor. The inputs are shown above the corresponding outputs for both the checkerboard test and the synthetic anomaly test. The input of the synthetic anomaly test is described in the caption of Fig. 4

Also, a high-attenuation anomaly, located in the center of the bay and as deep as 4 km, can be obtained by the inversion of real data.

5 Results and Joint Interpretation with the Geological and Geophysical Results

Figure 5 shows four horizontal slices through the velocity and attenuation models down to a depth of 4 km (left-hand and central columns). Figure 6b, c shows two vertical sections of these models, following the WE and SN directions as shown in Fig. 3 (gray dotted line). The P -wave percent velocity variations ($\% \Delta V_p$) are calculated by the P -wave velocity model of Zandomenighi et al. (2009). The interpretation of our results is based on the analysis of the largest attenuation anomalies in the regions of major volcanological interest (Fig. 7).

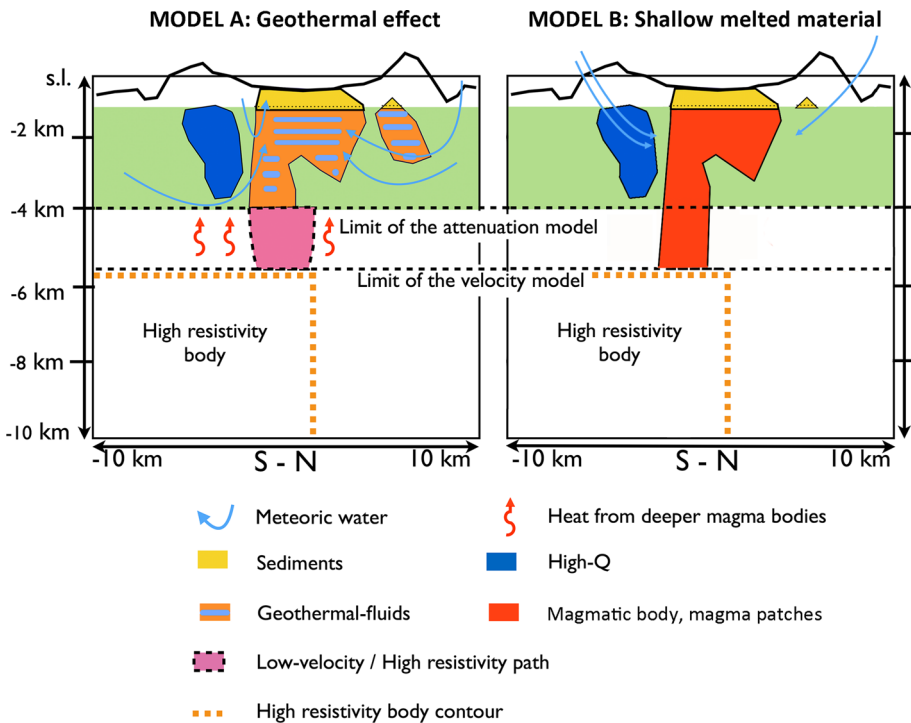


Fig. 7 Schematic interpretation of the attenuation model, carried out with reference to the 3D velocity (Zandomenighi et al. 2009) and resistivity (Pedrera et al. 2012) models, and constrained by other geophysical, geological, and geochemical observations, as described in the text. In the *upper-right* panel, we show a horizontal section of the region taken at 8 km depth and depicting the portion of the Bransfield Trough as well as the horizontal contour of the high-resistivity anomaly contained in the region under study. We also infer from our analysis both meteoric water circulation in the upper crust and heat rising toward the surface. We depict the depth dependence of the anomalies described in the text on two vertical sections, taken between depths of 0 and 10 km and crossing the Island (*gray dotted lines* in Fig. 3). Below a depth of 4 km, the sketch is based on the 3D velocity and resistivity results only. Below 5.5 km the sketch is based on the resistivity model only

In order to correlate the velocity and attenuation anomalies with those obtained by other geophysical and geological studies, we discuss the results under the Oceanic Crust and caldera structure separately from the ones under the Port Foster. We also separate the discussion of the anomalies under Port Foster bay in two different depth ranges (between depths of 1 and 2 km and between depths of 3 and 4 km).

5.1 Oceanic Crust and Caldera Structure

No unique high-attenuation anomaly larger than 2 km is visible under the Oceanic Crust contouring the island. An arc-shaped volume of small (2 km average dimension) high-attenuation anomalies is located northeast of Deception at a depth of 1 km (Fig. 5). This volume, located in a low-velocity zone, is partially visible in the 2 km tomograms. Zandomeneghi et al. (2009) interpret the vast superficial low-velocity anomaly northeast of the island (1–2 km depth, Fig. 5, left-hand column) as a zone of accumulation for sedimentary materials and hydrothermal activity. From the depth extension and location of the high-attenuation arc-shaped volume, we confirm this interpretation, in the sense that the high-attenuation anomaly may actually locate the inner boundary of the sedimentary structures and hydrothermal interactions.

Most of the source energy recorded near this boundary crosses the Port Foster bay, that is, the most attenuating structure in the entire region (Vila et al. 1995; Martinez-Arevalo et al. 2003). The fractured caldera as well as the faults contouring the inner bay may also reflect or diffract direct energy. Hence, we may not expect to image the exact lateral extension of these sediments. We may safely assume that velocity tomography provides more reliable information on these structures.

Under the south–southeastern part of the caldera structure, which constitutes the part of Deception emerged out of the Ocean, we observe the largest attenuation contrast, marking the entire depth range (e.g., Figs. 6c, 7 SN). The low attenuation visible under the caldera defines an almost vertical boundary with the high-attenuation medium under Port Foster, in strong correlation with the location of deep normal faults. The southern part of Deception is also affected by large smearing (Fig. 6d), induced by the large velocity contrast affecting the deep geometry of each source–station ray passing through it.

Pedraza et al. (2012) obtain a vast conductive body extending SE of the Island between depths of 2 and 12 km. The authors suggest emplacement of melt in this volume driven by an ENE–WSW oriented and SSE dipping regional normal fault. An almost vertical low-velocity and high-resistivity anomaly between depths of 2 and 6 km is located below Port Foster, connecting the vast southeastern high-resistivity anomaly with the center of the island. The vertical attenuation contrast is laterally disposed above the northwestern limit of the deep high-resistivity anomaly (Fig. 7).

Our results are compatible with previous studies (Ben-Zvi et al. 2009; Zandomeneghi et al. 2009; Pedraza et al. 2012) affirming that the south–southeastern part of the Island may contain a certain volume of a fluid/melt which may be the feeding path for the caldera. The section of this path, which should be connected to the center of the island and present high attenuation, reduces to our node spacing in the attenuation images at 4 km depth (Fig. 5, 4 km). Additionally, our results are also compatible with other interpretation provided by Martí et al. (2013) in which the deep feeding structures may simply heat the upper crustal systems, where meteoric waters both penetrate and circulate producing the high-attenuation anomaly in the center of the caldera (Fig. 7).

Deception faces the Bransfield Trough from northwest (Martí et al. 2013). The collapsed part of its caldera structure corresponds to the northwestern margin of the Trough as

well as to both steep almost vertical normal faults and strong attenuation contrasts (Fig. 7, upper-right panel). Velocity and resistivity tomograms show clear low-velocity and high-resistivity connections of the upper anomalies with deeper vast high-resistivity regions, extending southeast of the island (Fig. 7, vertical section). Our results are in concordance with those obtained by Pedrera et al. (2012) which suggested that the feeding system, through which fluids and melt materials either pass or heat the upper crustal materials, starts southeast of the Island at around 6 km. The main connection with the surface rises almost vertically toward the southeastern margin of the Island (Zandomenighi et al. 2009; Pedrera et al. 2012), passing through the high-attenuation contrasts southeast of the Island (Fig. 7). We discuss in the next two sections if, how, and where the deep melt materials are stored in the first 4 km under Deception.

5.2 From Depths of 1–2 km Under Port Foster

The Port Foster bay (inner bay of Deception Island, Fig. 1) is dominated by a large ΔQ_p^{-1} positive anomaly, that is, by high attenuation, down to a depth of 2 km (Fig. 5, central column, red). In this depth range, the high-attenuation volume is contoured by average-to-low-attenuation structures, mainly corresponding to the exposed caldera rim (Figs. 5, 6c). Zandomenighi et al. (2009) and Luzón et al. (2011) both propose that unconsolidated volcanoclastic and volcano-sedimentary materials, possibly producing high attenuation, extend down to 1.2–1.4 km depth. We remark that the anomaly in the center of the bay shows much higher attenuation than the surroundings. This is particularly relevant if we compare the results in the central bay with the arc of high attenuation located northeast of the island, where low velocities are also interpreted as induced by sediments (Zandomenighi et al. 2009).

The strong *P*-wave attenuation is paired with a strong scattering signature (obtained by Prudencio et al. 2013 under the bay) and suggests that materials with higher attenuation capacity than sediments, like hydrothermal interactions, intrude the first 2 km depth under the Port Foster bay. The top of a resistivity anomaly obtained by Pedrera et al. (2012) resembles pretty well the low-velocity and high-attenuation structure under the bay at a depth of 2 km (Fig. 5, see also Zandomenighi et al. 2009).

Getting *S*-wave velocity information is important for the interpretation of the attenuation anomalies. Luzón et al. (2011) provide us information on the transverse velocity wave field between depths of 1 and 2 km. The lowest *S*-wave velocities (related in the interpretation of Luzón et al. (2011) to the alterations produced by hydrothermal activity) are near the Chilean station (Fig. 1) northeast of the bay. On the contrary, the largest velocities occur near the SW caldera border, revealing the presence of compact materials at shallow depths. The low-velocity anomaly obtained by Luzón et al. (2011) at 1 km matches with the high-attenuation unique anomaly shifted toward the north part of the bay.

De Siena et al. (2010) depict zones of fluid accumulation coupled to a surrounding network of normal faults beneath Pozzuoli (Campi Flegrei, Italy), where the correlation of high attenuation and high V_p/V_s anomalies (Vanorio et al. 2005) is striking. This high-attenuation anomaly is contoured by a hard rock volume and associated with the caldera rim structure. This image is very similar to the one we observed at Deception (compare our results with De Siena et al. 2010, Fig. 7c, markers X4, X5, and X6). In De Siena et al. (2010), the presence of melt is restricted to a small volume located at a depth of about 4 km embedded in a hard rock volume, and heating the geothermal system under Pozzuoli.

The lateral extension of the high-attenuation anomaly at Deception is actually coincident with the Bathymetry of the floor of the bay (Fig. 6a), which reveals a broad uplift of the eastern side of the caldera (Cooper et al. 1999). As proposed by Barclay et al. (2009), bathymetric results could be caused by sediment supply rates and hydrothermal alterations from the east of the island or by a trapdoor caldera deformation with its minimum subsidence in the east. Both these causes are compatible with permeation of local meteoric water and seawater in the intra-caldera formation.

Other additional evidences of the nature of sediment deposits, volcanoclastic materials and hydrothermal alteration effects on the first 2 km shallow part of the caldera floor, are obtained by the study of some geochemical aspects of the area as the study of isotopes and noble gas data from fumarolic and bubbling gases and hot spring waters (Kusakabe et al. 2009). He and CO₂ are mainly of mantle origin, with no contribution of magmatic water to water and gas samples, hot spring fluids being a mixture of local meteoric water and seawater. Kusakabe et al. (2009) infer that these results are due to the existence of a heated hydrothermal system, with different temperatures in the depth range between 1 and 2 km.

The shape of the high-attenuation anomaly, contoured by the low-attenuation caldera rim between depths of 1 and 2 km (Figs. 5, 6), is similar to the one retrieved under different calderas and associated with the presence of hydrothermal alteration. The large low-velocity and high-attenuation structure in the bay (Figs. 5, 6b,c) correlates well with high resistivity, high scattering attenuation, and low *S*-wave velocities. Therefore, the attenuation anomaly shows a portion of the collapsed caldera center permeated by a geothermal reservoir, at least between depths of 1 and 2 km.

5.3 From Depths of 3–4 km Under Port Foster

Low-velocity and high-attenuation anomalies are less strong at depths larger than 2 km under Port Foster (Figs. 5, 6). The percent velocity variations show a continuous vertical anomaly between depths of 3 and 4 km, while the high-attenuation anomaly is shaped as a spherical-like system having its base approximately at 3 km depth (Fig. 6b, c). No large unique high-attenuation anomaly is visible at a depth of 4 km in the center of the bay (Figs. 5, 6c). High-attenuation anomalies with lateral extensions of the order of our node spacing connect the upper high-attenuation semi-spherical anomaly with depth. Our assumption is that seismic attenuation is more sensitive to the presence of deep melt and fluids than seismic velocity, while velocity tomography is able to sample larger depths (Hansen et al. 2004; De Siena et al. 2010; Muksin et al. 2013).

In their 2D and 3D resistivity maps, Pedrera et al. (2012) also reveal an ENE-WSW elongated conductor located between 2 and 6 km depth beneath the Port Foster bay, which they interpret as induced by a combination of partial melt and hot fluids. The depth resolution of the magnetotelluric model, which defines quite precisely the top of melt/fluid regions, is affected by the resistivity of the superficial highly resistive marine layers. This may cause an incorrect depth definition of the highly resistive structures. As in attenuation tomography, we use ray-dependent measurements to provide higher resolution than in magnetotelluric imaging, again at the expense of depth sampling.

The attenuation tomograms clearly show that the anomaly extends down to a maximum depth of 3 km as a unique hemispherical body. The depth extension and shape of the high-attenuation anomaly at depths of 3–4 km is similar to the ones observed in other areas, e.g., by De Siena et al. (2010) in the Campi Flegrei caldera, by Muksin et al. (2013) in the Tarutung Basin, and by Bohm et al. (2013) in the Kendeng Basin. These observations are always related to sedimentary or volcanoclastic deposits overlying active geothermal and gas

reservoirs. However, other studies interpret this high-attenuation anomaly and low-velocity body as the presence of a shallow partially melted magma body such as Koulakov et al. (2009) and Jaxybulatov et al. (2014) in Toba caldera or Ohlendorf et al. (2014) in Okmok Volcano. In Okmok volcano, the authors found the same pattern of velocity and attenuation observed in Deception Island and they interpreted the shallow part of the anomaly (surface to 2 km) as caldera fill, groundwater and small pods of magma and the deeper part of the anomaly (from 4 to 6 km) as a magma storage zone. This geodynamic model is compatible with the subduction processes or slab rollback suggested by Maestro et al. (2007).

As indicated previously in Sect. 2 and above, our results are compatible with both proposed models. The modeled volume of melted rocks of Ben-Zvi et al. (2009) (<15–20 km³) in depth can coexist with other effects as a network of magma and fluid filled batches of size either lower than or equal to our resolution seem the more reliable explanation for the absence of a unique high-attenuation anomaly down to 4 km. This network could be visible as a unique velocity and conductive anomaly, which may provide the main heat source that sustains the geothermal system in the first 3 km of the crust (Martí et al. 2013).

6 Conclusions

In the present work, we obtain the 3D *P*-wave attenuation model of Deception Island by using coda normalization method. The methodology used in this study is stable, robust, and reliable. The reliability of the method is based on the similarity of results with other studies. The study of *S*-waves and V_p/V_s distribution might better constrain the inner structure of the island.

We have provided new results showing the complex attenuative structure of the island with the presence of bodies of low and high attenuation. As in the velocity tomography, we find a limitation in the range of depth that we are able to solve due to the structure of the thinned oceanic crust region where the Moho is at 4–5 km depth and it implies a physical barrier.

One of the most important remarks is the presence of a high-attenuation body in the center of the island which extends from the surface to our resolution limit. The interpretation of this anomaly in the first two kilometers agrees with almost all researchers who have worked on the island and is associated with the effects of sedimentary and volcanoclastic deposits, hydrothermal interactions, and highly fractured material.

The interpretation of the deeper structure is more complex, mainly due to the lack of *S*-waves data. Thus, our results are consistent with two possible models. In the first, the high attenuation and low velocity is due to a hydrothermal system effects. On the other, this anomaly is interpreted as the existence of a partially molten magmatic body. A combination of these two models is also compatible with our results. It will be necessary to continue working to incorporate data from *S*-waves or other methodologies to give light to the interpretations.

Acknowledgments We gratefully acknowledge the Editor in Chief, Prof. Rycroft, Prof. Joan Martí, and one anonymous reviewer whose useful suggestions greatly improved the manuscript. This work has been partially supported by the Spanish Project Ephesos, CGL2011-29499-C02-01; by the EU Project EC-FP7 MEDiterranean SUPersite Volcanoes (MED-SUV); by the Basque Government researcher training program BF109.277; and by the Regional project ‘Grupo de Investigación en Geofísica y Sismología de la Junta de Andalucía, RNM104’. Edoardo del Pezzo has been partly supported by DPC-INGV projects UNREST,

SPEED and V2 (Precursori). We also thank Christine Thomas, Ralf Hetzel, and Stephan Klemme for the important suggestions regarding both the method and the interpretation.

References

- Aki K, Richards P (1980) Quantitative seismology—theory and methods. W. H. Freeman, San Francisco
- Almendros J, Ibáñez JM, Alguacil G, Del Pezzo E, Ortiz R (1997) Array tracking of the volcanic tremor source at Deception Island, Antarctica. *Geophys Res Lett* 24:3069–3072
- Barclay A, Wilcock WSD, Ibáñez JM (2009) Bathymetric constraints on the tectonic and volcanic evolution of Deception Island Volcano, South Shetland Islands. *Antarct Sci* 21:153–167. doi:[10.1017/S0954102008001673](https://doi.org/10.1017/S0954102008001673)
- Ben-Zvi T, Wilcock WSD, Barclay A, Zandomenighi D, Ibáñez JM, Almendros J (2009) The P wave velocity structure of Deception Island, Antarctica, from two dimensional seismic tomography. *J Volcanol Geotherm Res* 180:67–80
- Benítez MC, Ramírez J, Segura JC, Ibáñez JM, Almendros J, García-Yeguas A, Cortés G (2007) Continuous HMM-based seismic-event classification at Deception Island, Antarctica. *Geosci Remote Sens IEEE Trans* 45:138–146
- Berrococo M, Prates G, Fernández-Ros A, García A (2012) Normal vector analysis from GNSS–GPS data applied to deception volcano surface deformation. *Geophys J Int* 190:1562–1570
- Bohm M, Haberland C, Asch G (2013) Imaging fluid-related subduction processes beneath Central Java (Indonesia) using seismic attenuation tomography. *Tectonophysics* 590:175–188
- Calvet M, Margerin L (2013) Spatial variations of seismic attenuation in the Pyrenees: Coda Q and peak delay time analysis. *Bull Seismol Soci Am* 103. doi:[10.1785/0120120239](https://doi.org/10.1785/0120120239)
- Carmona E, Almendros J, Peña JA, Ibáñez JM (2010) Characterization of fracture systems using precise array locations of earthquake multiplets: an example at Deception Island volcano, Antarctica. *J Geophys Res Solid Earth* 115:1–20. doi:[10.1029/2009JB006865](https://doi.org/10.1029/2009JB006865)
- Carmona E, Almendros J, Serrano I, Stich D, Ibáñez JM (2012) Results of seismic monitoring surveys of Deception Island volcano, from 1999–2011. *Antarct Sci* 24:485–499. doi:[10.1017/S0954102012000314](https://doi.org/10.1017/S0954102012000314)
- Carmona E, Almendros J, Martín R, Cortés G, Alguacil G, Moreno J, Martín JB, Martos A, Serrano I, Stich D, Ibáñez JM (2014) Advances in seismic monitoring at Deception Island Volcano (Antarctica) since the international polar year. *Ann Geophys* 57(3). doi:[10.4401/ag-6378](https://doi.org/10.4401/ag-6378)
- Caselli A, Santos-Alfonso M, Agosto MR (2004) Gases fumarólicos de la isla Decepcion (Shetland del Sur, Antartida): variaciones químicas y depositos vinculados a la crisis sismica de 1999. *Asociación Geológica Argentina Revista* 59:291–302
- Caselli A, Badi G, Bonatto AL, Bengoa CL, Agosto MR, Bidone A, Ibáñez JM (2007) Actividad sísmica y composición química fumarólica anómala debido a posible efecto sello en el sistema volcánico, Isla Decepción (Antártida). *Revista de la Asociación Geológica Argentina* 62:545–552
- Catalán M, Agudo LM, Muñoz-Martín A (2006) Geomagnetic secular variations of Bransfield Strait (Western Antarctica) from analysis of marine crossover data. *Geophys J Int* 165:73–86
- Chouet B (2003) Volcano seismology. *PAGEOPH* 160:739–788
- Cooper AP, Smellie JL, Maylin J (1999) Evidence for shallowing and uplift from bathymetric records of Deception Island, Antarctica. *Antarct Sci* 10:455–461
- De Siena L, Del Pezzo E, Bianco F, Tramelli A (2009) Multiple resolution seismic attenuation imaging at Mt. Vesuvius. *Phys Earth Planet Inter* 173:17–32
- De Siena L, Del Pezzo E, Bianco F (2010) Seismic attenuation imaging of Campi Flegrei: evidence of gas reservoirs, hydrothermal basins and feeding systems. *J Geophys Res* 115:B09312. doi:[10.1029/2009JB006938](https://doi.org/10.1029/2009JB006938)
- De Siena L, Del Pezzo E, Thomas C, Curtis A, Margerin L (2013) Seismic energy envelopes in volcanic media: in need of boundary conditions. *Geophys J Int* 195(2):1102–1119. doi:[10.1093/gji/ggt273](https://doi.org/10.1093/gji/ggt273)
- De Siena L, Thomas C, Aster R (2014) Multi-scale reasonable attenuation tomography analysis (MuRAT): an imaging algorithm designed for volcanic regions. *J Volcanol Geotherm Res* 277:22–35
- Del Pezzo E (2008) Seismic wave scattering in volcanoes. *Adv Geophys* 50:353–371
- Del Pezzo E, Bianco F, De Siena L, Zollo A (2006) Small scale shallow attenuation structure at Mt. Vesuvius. *Phys Earth Planet Inter* 157:257–268
- Eberhart-Phillips D, Reyners M, Chadwick M, Stuart G (2008) Three-dimensional attenuation structure of the Hikurangi subduction zone in the central North Island, New Zealand. *Geophys J Int* 174:418–434

- Fernández-Ibáñez F, Pérez-López R, Martínez-Díaz JJ, Paredes C, Giner-Robles J, Caselli A, Ibáñez JM (2005) Costa Recta beach, Deception Island, West Antarctica: a retreated scarp of a submarine fault. *Antart Sci* 17:418–426
- García-Yeguas A, Almendros J, Abella R, Ibáñez JM (2010) Quantitative analysis of seismic wave propagation anomalies in azimuth and apparent slowness at Deception Island volcano (Antarctica) using seismic arrays. *Geophys J Int*. doi:10.1111/j.1365-246X.2010.04864.x
- Haberland C, Rietbrock A (2001) Attenuation tomography in the western central Andes: a detailed insight into the structure of a magmatic arc. *J Geophys Res* 106(B6):11,151–11,167
- Hansen S, Thurber CH, Mandernach M, Haslinger F, Doran C (2004) Seismic velocity and attenuation structure of the east rift zone and south flank of Kilauea Volcano, Hawaii. *Bull Seismol Soc Am* 94:1430–1440
- Hunsen S, Smith RB, Waite GP (2004) Evidence for gas and magmatic sources beneath Yellowstone volcanic field from seismic tomographic imaging. *J Volcanol Geotherm Res* 131:397–410
- Ibáñez JM, Almendros J, Alguacil G, Morales J, Del Pezzo E, Ortiz R (1997) Eventos sísmicos de largo período en la isla de Deception: evidencias de una zona volcánica activa. *Boletín de la RSEHN* 93:103–110
- Ibáñez JM, Del Pezzo E, Morales J, Alguacil G, Almendros J, Ortiz R, La Rocca M, García A (2000) Seismovolcanic signals at Deception Island volcano, Antarctica: wave field analysis and source modeling. *J Geophys Res* 135:13,905–13,931
- Ibáñez JM, Carmona E, Almendros J, Saccorotti G, Del Pezzo E, Abril M, Ortiz R (2003) The 1998–1999 seismic series at Deception Island volcano, Antarctica. *J Volcanol Geotherm Res* 128:65–88
- Jaxybulatov K, Shapiro NM, Koulakov I, Mordret A, Lands M, Sens-Schonfelder C (2014) A large magmatic sill complex beneath the Toba caldera. *Science* 346:617–619
- Julian BR, Ross A, Foulger GR, Evans JR (1996) Three-dimensional seismic image of a geothermal reservoir: the Geysers, California. *Geophys Res Lett* 23:685–688
- Julian BR, Pitt A, Foulger GR (1998) Seismic image of CO₂ reservoir beneath a seismically active volcano. *Geophys J Int* 133:F7–F10
- Koulakov I, Yudistira T, Luehr BG (2009) P, S velocity and VP/VS ratio beneath the Toba caldera complex (Northern Sumatra) from local earthquake tomography. *Geophys J Int* 117(3):1121–1139
- Koulakov I, Bindi D, Parolai S, Gresser H, Milkereit C (2010) Distribution of seismic velocities and attenuation in the crust beneath the North Anatolian Fault (Turkey) from local earthquake tomography. *Bull Seismol Soc Am* 100(1):207–224
- Kusakabe M, Nagao K, Ohba T, Hun Seo J, Park S, Lee J, Park B (2009) Noble gas and stable isotope geochemistry of the thermal fluids from Deception Island, Antarctica. *Antart Sci* 21:255–267
- Kuznetsov P, Koulakov I (2014) The three-dimensional structure beneath the Popocatepetl volcano (Mexico) based on local earthquake seismic tomography. *J Volcanol Geotherm Res* 276:10–21
- La Rocca M, Del Pezzo E, Simini M, Scarpa R, De Luca G (2001) Array analysis of seismograms for explosive sources: evidence for surface waves scattered at the main topographical features. *Bull Seismol Soc Am* 91:219–231
- Lees JM, Lindley GT (1994) Three-dimensional attenuation tomography at Loma Prieta: inverting t^* for Q . *J Geophys Res* 99(B4):6843–6863
- Luzón F, Almendros J, García-Jerez A (2011) Shallow structure of Deception Island, Antarctica, from correlations of ambient seismic noise on a set of dense seismic arrays. *Geophys J Int* 185:737–748
- Maestro A, Somoza L, Rey J, Martínez-Fras J, López-Martínez J (2007) Active tectonics, fault patterns and stress field of Deception Island: a response to oblique convergence between the Pacific and Antarctic plates. *J S Am Earth Sci* 23:256–268
- Martí J, Vila J, Rey J (1996) Deception Island (Bransfield Strait, Antarctica): an example of a volcanic caldera development by extensional tectonics. In: McGuire WJ, Jones AP, Neuberg J (eds) *Volcano instability on the Earth and other planets*. Special Publication of the Geological Society, London, pp 253–265
- Martí J, Geyer A, Aguirre-Díaz G (2013) Origin and evolution of the Deception Island caldera (South Shetland Islands, Antarctica). *Bull Volcanol* 75:732–750
- Muñoz Martín A, Catalan M, Martín J, Carbo A (2005) Upper structure of Deception Island area (Bransfield Strait, Antarctica) from gravity and magnetic modelling. *Antart Sci* 17:213–224
- Martínez-Arevalo C, Bianco F, Ibáñez JM, Del Pezzo E (2003) Shallow seismic attenuation and shear-wave splitting in the short-period range of Deception Island volcano (Antarctica). *J Volcanol Geotherm Res* 128:89–113
- Matsumoto S, Uehira K, Watanabe A, Goto K, Iio Y, Hirata N, Okada T, Takahashi H, Shimizu H, Shinohara M, Kanazawa T (2009) High resolution Q^{-1} estimation based on extension of coda normalization method and its application to P-wave attenuation structure in the aftershock area of the 2005 West Off Fukuoka Prefecture Earthquake (M 7.0). *Geophys J Int* 179:1039–1054

- Melo R, Vieira G, Caselli A, Ramos M (2012) Susceptibility modelling of hummocky terrain distribution using the information value method (Deception Island, Antarctic Peninsula). *Geomorphology* 155–156:88–95
- Morozov IB (2011) Mechanisms of geometrical seismic attenuation. *Ann Geophys* 54(3). doi:[10.4401/ag-4780](https://doi.org/10.4401/ag-4780)
- Muksin U, Haberland C, Bauer K, Weber M (2013) Three-dimensional upper crustal structure of the geothermal system in Tarutung (North Sumatra, Indonesia) revealed by seismic attenuation tomography. *Geophys J Int* 195. doi:[10.1093/gji/ggt383](https://doi.org/10.1093/gji/ggt383):2037–2049
- Ohlendorf SJ, Thurber C, Pesicek JD, Prejean SG (2014) Seismicity and seismic structure at Okmok Volcano, Alaska. *J Volcanol Geotherm Res* 278:103–119
- Ortiz R, García A, Aparicio A, Blanco I, Felpeto A, Del Rey R, Villegas MT, Ibáñez JM, Morales J, Del Pezzo E, Olmedillas J, Astiz MM, Vila J, Ramos M, Viramonte JG, Risso C, Caselli A (1997) Monitoring of the volcanic activity of Deception Island, South Shetland Islands, Antarctica (1986–1995). In: Ricci CA (ed) *The Antarctic region: geological evolution and processes*. Terra Antarctica Publications, Siena, pp 1071–1076
- Pedraza A, Ruíz-Constán A, Heredia N, Galindo-Zaldívar J, Bohoyo F, Marín-Lechado C, Ruano P, Somoza L (2012) The fracture system and the melt emplacement beneath the Deception Island active volcano, South Shetland Islands, Antarctica. *Antarct Sci* 24:173–182
- Prates G, Berrocoso M, Fernández-Ros A, García A (2013) Enhancement of sub-daily positioning solutions for surface deformation monitoring at Deception volcano (South Shetland Islands, Antarctica). *Bull Volcanol* 75:1–10
- Priyono A, Suantika G, Widiyantoro S, Nugraha AD (2011) Three-dimensional seismic attenuation structure of Mt. Guntur, West Java, Indonesia. *Int J Tomogr Simul* 17:17–28
- Prudencio J, Ibáñez JM, García-Yeguas A, Del Pezzo E (2013) Spatial distribution of intrinsic and scattering seismic attenuation in active volcanic islands, II: Deception Island images. *Geophys J Int* 195(3):1957–1969. doi:[10.1093/gji/ggt360](https://doi.org/10.1093/gji/ggt360)
- Saccorotti G, Almendros J, Carmona E, Ibáñez JM, Del Pezzo E (2001) Slowness anomalies from two dense seismic arrays at Deception Island volcano, Antarctica. *Bull Seismol Soc Am* 91:561–571
- Sato H, Fehler MC, Maeda T (2012) *Seismic wave propagation and scattering in the heterogeneous earth*, 2nd edn. Springer, New York
- Schurr B, Asch G, Rietbrock A, Trumbull R, Haberland CH (2003) Complex patterns of fluid and melt transport in the central Andean subduction zone revealed by attenuation tomography. *Earth Planet Sci Lett* 215:105–119
- Smellie JL (2001) Lithostratigraphy and volcanic evolution of Deception Island, South Shetland Islands. *Antarct Sci* 13:118–209
- Smellie JL, López-Martínez J, Headland RK, Hernández-Cifuentes F, Maestro A, Millar IL, Thomson JW (2002) *Geology and geomorphology of Deception Island*. British Antarctic Survey, Cambridge, 77 pp
- Takanami T, Selwyn Sacks I, Hasegawa A (2000) Attenuation structure beneath the volcanic front in northeastern Japan from broad-band seismograms. *Phys Earth Planet Inter* 121:339–357
- Tejedo P, Gutiérrez B, Pertierra LR, Benayas J (2014) Analysis of published scientific research from Deception Island, South Shetland Islands. *Antarct Sci*. doi:[10.1017/S0954102014000455](https://doi.org/10.1017/S0954102014000455)
- Torrecillas C, Berrocoso M, Pérez-López R, Torrecillas M (2012) Determination of volumetric variations and coastal changes due to historical volcanic eruptions using historical maps and remote-sensing at Deception Island (West-Antarctica). *Geomorphology* 136:6–14
- Torrecillas C, Berrocoso M, Felpeto A, Torrecillas M, García A (2013) Reconstructing palaeo-volcanic geometries using a Geodynamic Regression Model (GRM): application to Deception Island Volcano (South Shetland Islands, Antarctica). *Geomorphology* 182:79–88
- Vanorio T, Virieux J, Capuano P, Russo G (2005) Three-dimensional tomography from P wave and S wave microearthquake travel times and rock physics characterization of the Campi Flegrei Caldera. *J Geophys Res* 110(B03201). doi:[10.129/2004JB003102](https://doi.org/10.129/2004JB003102)
- Vila J, Martí J, Ortiz R, García A, Correig AM (1992) Volcanic tremors at Deception Island, South Shetland Islands, Antarctica. *J Volcanol Geotherm Res* 53:1–4
- Vila J, Correig AM, Martí J (1995) Attenuation source parameters at Deception Island (South Shetland Islands, Antarctica). *Pure Appl Geophys* 144:229–250
- Yoshimoto K, Sato H, Ohtake M (1993) Frequency-dependent attenuation of P and S waves in Kanto area, Japan, based on the coda-normalization method. *Geophys J Int* 114:165–174
- Zandomenghi D, Barclay A, Almendros J, Ibáñez JM, Wilcock WSD (2009) Crustal structure of Deception Island volcano from P-wave seismic tomography: tectonic and volcanic implications. *J Geophys Res* 114:B06310. doi:[10.1029/2008JB006119](https://doi.org/10.1029/2008JB006119)